Crowdsourcing air temperature data for the evaluation of the urban microscale model PALM – a case study in central Europe

Lara van der Linden[1,2]*, Patrick Hogan[2], Björn Maronga[3], Rowell Hagemann[2], Benjamin Bechtel[1]

[1] Institute of Geography, Ruhr-University Bochum, Bochum, Germany

[2] Lohmeyer GmbH, Bochum, Germany

[3] Institute of Meteorology and Climatology, Leibniz University Hannover, Hannover, Germany

* Corresponding author

E-mail: lara.vanderlinden@rub.de

Abstract

In summertime and during heat events the urban heat island can negatively impact public health in urban areas. In the context of climate change, climate adaptation receives more attention in urban planning. Microscale urban climate modelling can identify risk areas and evaluate adaptation strategies. Concurrently, evaluating the model results with observational data is essential. So far, model evaluation is mostly limited to short-term field campaigns or a small number of stations. This study uses novel crowdsourcing data from Netatmo citizen weather stations (CWS) to evaluate the urban microscale model PALM for a hot day ($T_{max} \geq 30$ °C) in Bochum in western Germany with anticyclonic atmospheric conditions. Urban-rural air temperature differences are represented by the model. A quality control procedure is applied to the crowdsourced data prior to evaluation. The comparison between the model and the crowdsourced air temperature data reveals a good model performance with a high coefficient of determination (R^2) of 0.86 to 0.88 and a root mean squared error (RMSE) around 2 K. Model accuracy shows a temporal pattern and night-time air temperatures during the night are underestimated by the model, likely due to unresolved cloud cover. The crowdsourced air temperature data proved valuable for model evaluation due to the high number of stations within urban areas. Nevertheless, weaknesses related to data quality such as radiation errors must be considered during model evaluation and only the information derived from multiple stations is suitable for model evaluation. The procedure presented here can easily be transferred to planning processes as the model and the crowdsourced air temperature data are freely available. This can contribute to making informed decisions for climate adaptation in urban areas.

Introduction

Cities are a central part of human life, providing space for living, work and services. Over the last decades, the amount of people dwelling in cities globally increased significantly. In 1950, only 30% of the world's population resided in cities. By 2018, this fraction increased to 55% and a further increase to 68% is projected in 2050 [1]. This urbanisation process alters social and economic structures [1] as well as transforms the natural environment into an urban environment [2].

The transformation of natural into urban surfaces has multiple effects on the environment resulting in an urban ecosystem. Modifications of the urban atmosphere ensue from changes in the albedo and emissivity of surfaces, modified evaporation rates, aerodynamic roughness and the composition of the atmosphere in terms of water vapour, gases and particulate matter [2]. One atmospheric alteration resulting from the urbanisation process is the canopy layer urban heat island (CLUHI). It describes the relative overheating of the urban atmosphere in comparison to rural areas [2–5]. Combining this with warm and/or hot weather, this urban overheating can affect the health and comfort of a cities' population due to thermal stress [4,6–8]. Past heatwaves, like the one in Europe in 2003, have caused thousands of additional deaths due to heat-related mortality [9]. The CLUHI represents an additional risk factor as it increases the heat load [7,9].

Anthropogenic climate change has the potential to further increase the risk of heat-related mortality. By 2020, the global air temperature has increased by 1.09 °C compared to pre-industrial levels [10]. The rise in air temperatures is not globally uniform as the mean air temperature, e.g., in Germany has increased by 1.6 °C since 1881 [11]. Furthermore, climate change is affecting extreme weather events like hot extremes. Since the 1950s, the occurrence of hot extremes has increased almost globally and human influence has contributed to the increase with medium to high confidence in many regions [10]. Additionally, the increase in the frequency of hot days and nights is accentuated in urban areas compared to rural areas [12]. A further rise in the occurrence of hot extremes is projected [10]. The CLUHI, rising air temperatures and higher frequency of heatwaves due to climate change aggregate and lead to an increased heat load and additional heat stress for urban populations [6,13].

All the factors listed above raise the need for adaptation to changing climatic conditions in cities. City planners require detailed information on the urban microclimate to identify risk areas and plan adaptation strategies and evaluate different adaptation strategies [6,14–18]. Numerical models can calculate the urban microclimate in the required resolution under current conditions and enable comparative studies to evaluate different strategies [8,14,16].

Today, various models are available to simulate the urban climate at different scales. At the microscale computational fluid dynamics (CFD) models are frequently used. CFD models combine temperature and velocity fields and enable accurate modelling of the urban microclimate with relevant processes such as turbulent flow, exchange of latent and sensible heat and radiative transfer [14,19]. This qualifies them as a common tool to evaluate human thermal comfort and exposure in cities [6,18]. At the same time, CFD models require detailed information on the urban structure and surface materials such as the exact position and height of buildings as well as boundary conditions and they demand significant computational resources [14,19].

One CFD model is the PALM model system which has recently been extended for urban applications with the PALM-4U model components [20]. The model core has been developed for more than 15 years as a parallelised large-eddy simulation model [21]. The newly developed modules for urban applications include a radiative transfer model, a building surface model, an indoor model, a surface spinup mechanism, a human biometeorology model with a multi-agent system as well as self- and offline nesting with mesoscale weather models [20]. A validation study in Prague revealed a good representation of the urban microclimate for a winter and a summer situation [19]. The model is sensitive to changes in surface properties and green infrastructure within a city [22,23]. Therefore, the model has proven relevant capability to model thermal exposure and thermal comfort in the urban environment facilitating the evaluation of adaptation strategies for urban planning [6,24]. However, case specific evaluation is still favourable to ensure its applicability under various conditions and in different surroundings.

Therefore, spatially resolved observations are needed. Data provided by professional weather stations have high installation and maintenance costs, and thus typically are not spatially dense enough to represent intraurban air temperature variations [25,26]. Intensive mobile measurement campaigns are still costly to maintain and implement and limited in spatial coverage [26,27]. An alternative to mobile and in-situ measurements is crowdsourcing. Due to the ever-increasing number of devices and sensors connected to the internet, observations of a variety of atmospheric quantities is available through crowdsourcing [26]. In recent years, citizen weather stations (CWS) produced by the company Netatmo have received increasing attention for the investigation of the CLUHI [27–32]. The data is freely accessible through an API [28]. As the placement of the sensors is not regulated, several quality control procedures have been developed and improved to ensure high data quality for research purposes [28,30,31]. The air temperature data have been applied to evaluate the CLUHI of cities and the air temperature differences on a local scale [29]. The data were combined with remote sensing data and machine learning algorithms such as Random Forest to model the air temperature for the city of Berlin [27].

The present study uses the urban microscale model PALM to model the thermal conditions of a hot day ($T_{max} \geq 30$ °C) in the city of Bochum, Germany. The model evaluation is based on a professional weather station and uses crowdsourced air temperature data from Netatmo CWS. The aim is to examine the usability of crowdsourced air temperature data for the evaluation of a micro-scale climate model. The following research questions shall be answered by this study: In the present study, does the PALM model display intraurban air temperature differences according to well-known principles of the urban climate? Based on the evaluation with CWS data, can a temporal and/or spatial pattern in model accuracy be detected? And finally, how suitable are CWS data for the evaluation of PALM?

Materials and Methods

Study area

The city of Bochum is located in western Germany in the polycentric urban area Ruhr encompassing 53 cities. In total, 5.1 million people live in the Ruhr area within an area of 4440 km^2 [33] characterised by a smooth transition between cities. Bochum is defined by a diverse structure of land use ranging from the densely built-up city centre to industrial and commercial sites to green areas spread over the city.

The study area encompasses the city centre, residential areas north and south of the city centre, a few commercial areas and a large park near the city centre and is characterised by a diverse structure (Fig 1). The dense city centre is surrounded by residential areas to the north and the south. To the west and the east, the urban structure is less dense with several commercial areas. At a further distance from the city centre, the urban structure is interrupted by open and natural areas. The terrain generally rises from the northwest to the southeast with an altitude ranging from 42 to 148 m above sea level. The smaller focus area, later called child domain, within the study areas highlights the northern city centre and the large park. The southern part of the focus area contains the dense city centre and the train tracks which encompass the city centre of Bochum. The train tracks are elevated from the surrounding areas. North of the train tracks the structure is less dense and impervious. Residential areas dominate interspersed with small commercial areas along the main roads. Two parks are located in the focus area: the smaller "Schmechtingwiesen Park" in the west and the larger "Stadtpark" in the east. South of Schmechtingwiesen Park are several allotments. Differences in elevation amount to about 50 m.

Fig 1. Location of the study area, building positions within the study area and land use classes provided to the PALM model; land use classes are grouped into pavement types, vegetation types and water.

Study period

As the CLUHI is most pronounced in summer in mid-latitude cities, a heatwave period in August 2020 was chosen as the study period. The heatwave lasted from the 5th of August to the 13th of August 2020. A 30-hour period starting on the night of the hottest day (the 8th of August) of this heatwave was chosen for the PALM simulation. According to the weather classification by the German Weather Service (DWD), central Europa was under the influence of high-pressure systems for the duration of the heatwave period, classified as BM (ridge of high pressure, central Europa) from the 5th of August to the 7th of August, as NEa (north-eastern weather situation, anticyclonic conditions central Europe) from the 8th of August to the 10th of August and as SEa (south-eastern weather situation, anticyclonic conditions central Europe) from the 11th of August to the 13th of August. A weak flow from the northeast transported warm and dry air towards central Europe during the simulated period from 8th of August 00:00 h to 9th of August 06:00 h [34].

The influence of the high-pressure system resulted in a maximum air temperature of 36.4 °C on the 8th of August as recorded by the professional weather station LMSS further described below. While during the first night the minimum air temperature reached 16 °C, air temperatures dropped only shortly below 20 °C in the second night. The mean relative humidity for the simulated period was 54.5 %. The overall wind speed was low with a mean of 1.4 ms^{-1} and a maximum wind speed of 7.3 ms^{-1} at 10 m above roof level.

Weather data

Professional weather station data

A professional weather station run by the urban climatology group at Ruhr-University Bochum is situated within the study area. The station "Ludger Mintrop Stadtklima Station" (LMSS), hereafter referred to as reference station, is located in the focus area. The 10 m wind tower is on top of a building in the city centre resulting in a measurement height of 37.8 m above ground. Air temperature and humidity as well as soil temperatures are recorded in an allotment south of Schmechtingwiesen Park. The sensors for air temperature and humidity are placed inside a radiation shield without artificial ventilation. Measurement range and accuracy for all sensors are listed in Table 1.

Table 1. Measurement range and accuracy of the relevant sensors at the professional weather station LMSS

Parameter	Measurement range	Measurement accuracy
Air temperature	-30 to 100 °C	± 0.1 °C
Relative humidity	10 to 100%	± 2%
Wind speed	0.3 to 15 m/s	± 0.3 m/s
	>15 to 50 m/s	± 2% of measurement

Crowdsourced air temperature data

CWS produced by the company Netatmo are the source for the crowdsourced air temperature data. The stations consist of an indoor and an outdoor module encased in a cylindrical aluminium shell. Data recorded by the outdoor module can be made available to the public. The outdoor module records air temperature and humidity [30]. The measured range of air temperature is -40 to +65 °C with an accuracy of ±0.3 °C and the range of relative humidity is 0 to 100% with an accuracy of ±3% [35]. A comparative measurement by Meier et al. [30] in a climate chamber confirms the air temperature accuracy except for low air temperatures of 0 °C. A field comparison revealed an accuracy of ±0.5 °C between 14:00 h and 05:00 h and a lower accuracy after sunrise and during morning hours of up to -1.3 K [30].

Data provided by Netatmo were extracted via the APIs and stored in a database. Stations received an internal ID. When relocated, a station receives a new ID to keep the time series consistent. Hourly mean values were accessed. The timestamp was modified to represent the end of the averaging interval [28]. A quality control (QC) procedure, first developed by Napoly et al. [31] and recently updated by Fenner et al. [28], was applied to the observations. The QC procedure filters stations and data points in five main steps:

1. Metadata check: duplicate stations are removed (M1)
2. Outlier detection based on a comparison of individual data points to the data distribution (M2)
3. Data validity check: if more than 20% of the data in a certain time period of an individual station is flagged in the previous step, this station is flagged (M3)
4. Identification of indoor stations by temporal correlation (M4)
5. Spatial buddy check: further identification of indoor stations and radiation errors (M5)

The optional QC level O1, a temporal interpolation for individual missing timesteps to increase data availability, was additionally applied to the database. Default settings for each QC level were used as presented in Fenner et al. [28], except for level M5. Isolated stations were not removed from the database. For this study, data for August 2020 was retrieved from the database. When combined with the model results, the dataset was filtered further based on whether a station provided more than 80 % of data for the study period. A total of 59 stations remained.

PALM model

Model configuration

The PALM model system 6.0 revision 4901 was applied in this evaluation study. PALM uses the incompressible Boussinesq approximations of the Navier-Stokes equations which calculate seven prognostic variables on a staggered Cartesian (Arakawa-C) grid: the velocity components *u*, *v* and *w*, the potential temperature, the subgrid-scale turbulence kinetic energy, the water vapour mixing ratio, and optionally a passive scalar. These variables are calculated by solving the equations for the conservation of mass, momentum, thermal internal energy, moisture, and the optional passive scalar

[20]. The turbulence closure on the subgrid scale followed the 1.5-order Deardorff's approach [36], further refined by Moeng and Wyngaard [37] and Saiki et al. [38]. Advection was described by the 5th order upwind scheme of Wicker and Skamarock [39]. Time was discretised by the 3rd order Runge-Kutta timestep scheme [40]. A multigrid pressure solver for the Poisson equation was applied. Boundary conditions at the surface are defined using the Monin-Obukhov similarity theory where a constant flux layer is assumed between the surface and the first grid level. Here roughness lengths for heat, humidity and momentum are used to provide surface heat fluxes of momentum, heat and moisture to the first grid level [20].

The PALM model includes several modules which extend the functionality of the model core to real-world scenarios. The relevant modules for this work are the land surface model (LSM), the radiation model, the radiative transfer model (RTM), the building surface model (BSM), the plant canopy model (PCM), the surface spinup mechanism, and the offline and online nesting implementation [20].

Interactions with the surface are provided by the LSM and inside of urban areas additionally by the BSM. The LSM solves the energy balance of natural surfaces like soils, vegetation types and water surfaces and paved surfaces like streets and pavements [20,41]. The BSM calculates the energy balance of building surfaces like walls, roofs, and windows. The energy balance is solved in the same way as in the land surface model, but the model is applied to vertical and horizontal surfaces [20,42]. The PCM accounts for the influence of the resolved vegetation on the radiation as well as dynamic and thermodynamic processes [20,42]. The built-in clear sky radiation model provides incoming and outgoing radiation fluxes and models the radiation budget at the surface [20]. The radiation model is extended with the RTM which models radiative processes in complex environments where shading and multiple reflections are important [43].

The surface spinup mechanism enables a precursor simulation of the radiation model, the LSM and BSM. As detailed information on surface and material temperatures are often unavailable, the spinup mechanism improves the information on initial material and ground temperatures and provide almost equilibrium conditions at model initialisation. The atmospheric code is switched off during the spinup which saves computational cost [20]. A spinup period of 24 hours was applied in this study.

PALM's offline and online nesting were utilised in the present study. Three model domains were defined to incorporate mesoscale weather effects and model microscale processes in the urban canopy. A mesoscale domain with a size of ~ 40 x 45 km and a resolution of 50 m horizontally was used in a precursor simulation to exclude turbulence adjustment zones from the study area. A vertical grid spacing of 25 m was used up to a height of 2000 m, followed by a grid stretching of 1.08 resulting in a vertical domain size of approx. 6000 m. The following simulation was divided into a parent and child domain. The parent domain had a size of 8.8 x 8.5 km with an isotropic grid spacing of 10 m. Vertical grid stretching was applied after 200 m resulting in a height of approx. 1300 m. The child domain covered an area of 1.8 x 1.5 km with an isotropic grid spacing of 2.5 m and 60 vertical grid levels. All domain layouts are represented in Fig 2.

Fig 2. Domain layouts of the mesoscale simulation (upper right) and the microscale simulation with parent and child domains as well as the available Netatmo stations in the study area.

Offline nesting allows to incorporate results from mesoscale weather prediction models as atmospheric boundary conditions. The pre-processor INIFOR, provided by PALM, calculates realistic initial and boundary conditions from the COSMO D2 model and provides it for the PALM simulation via the dynamic driver file [20]. COSMO-D2 was the weather forecast model used by the DWD [44]. The pre-processor transforms the COSMO rotated pole coordinates to the PALM Cartesian coordinates and then interpolates the COSMO data to the desired PALM resolution. It requires specific files: a file with the COSMO numerical grid, a file with the COSMO soil map to identify water cells and hourly files with COSMO analysis or forecast data for the atmospheric field and the soil temperature and moisture. Additionally, a namelist file is required which determines the domain setup and geographical position of the domain. Further options can be provided by the command-line options of the INIFOR call [45].

As the COSMO model is a RANS model, turbulence is not explicitly resolved, and turbulent fluctuations must be added to the boundary values. For this purpose, the synthetic turbulence generator was applied. It is based on a method by Xie and Castro [46] which adds perturbations to the wind components at the lateral boundaries [47].

Due to the computational cost of the large mesoscale model domain, it was impossible to directly nest the study area into the mesoscale domain. Therefore, the results of the mesoscale simulation were saved with a five-minute temporal resolution which includes the resolved turbulence. This output was then processed to serve as a dynamic driver for the following simulation where the boundary conditions are updated every five minutes. As turbulence is already resolved in the dynamic driver, the adjustment zones for the generation of turbulence in the parent domain could be reduced. The online nesting allows the simulation of a large domain with a coarse resolution combined with a small domain containing the area of interest with a fine resolution. The one-way coupled mode of the online nesting was applied here where influences from the parent domain are interpolated on the child domain without feedbacks from the child to the parent domain [48].

A detailed description of the model is given by Maronga et al. [20]. Further information on the model components can be found in Gehrke et al. [41] for the LSM, Resler et al. [42] for the BSM, Salim et al. [43] for the RTM, Kadasch et al. [47] for the offline nesting and Hellsten et al. [48] for the online nesting.

The mesoscale simulation was run on 126 CPU cores. The nested microscale simulations were run on 112 CPU cores with 64 CPU cores for the parent domain and 48 CPU cores for the child domain. The runtime for the mesoscale run was 27 hours and for the microscale runs was 11 days and 4 hours.

Urban canopy description

The static driver contains all information on the surface properties and topography of the model domains. The required information was derived from freely available datasets provided by the state of North Rhine-Westphalia, the Federal Republic of Germany or the Copernicus Land Monitoring Service. The data sources are listed in Table 2.

Table 2. Information on the datasets used as the basis for the static driver as model input

Dataset	Description	Resolution	Provider	Reference
DEM200	Digital elevation model as xyz dataset	200 m	Federal Republic of Germany	[49]

DEM	Digital elevation model as xyz dataset	1 m		[50]
3D laser scanning data	Measurement data from airborne laser scanning as laz dataset	4 to 10 points per m^2	State of North Rhine-Westphalia	[51]
3D building model LoD1	3D building model with buildings represented as blocks without roof shapes in CityGML format	Height accuracy: ±5 m		[52]
Urban Atlas 2018	Detailed land cover information for urban areas as ESRI shapefile	Minimum mapping units: class 1: 0.25 ha class 2 – 5: 1 ha	Copernicus Land Monitoring Service	[53]
CORINE land cover 2018	European land cover map as ESRI shapefile	Minimum mapping units: 25 ha		[54]

Input data for the mesoscale simulation were the DEM200 and the CORINE land cover datasets. The digital elevation model was resampled to a resolution of 50 x 50 m and the CORINE land cover dataset was rasterised. The CORINE land cover classes were translated into the PALM vegetation, pavement and water classes according to S1 Table.

Input data for the parent and child domains were the DEM, the 3D laser scanning data, the building model and the Urban Atlas data. The DEM was resampled to a resolution of 10 x 10 m for the parent domain and 2.5 x 2.5 m for the child domain. The Urban Atlas was rasterised, and the land cover classes were converted into PALM vegetation, pavement and water classes according to S2. Building heights were derived from the 3D building model. Each building was assigned an ID and a building type. In this study, PALM building type 2 (residential, 1950 to 2000) was used as data on the building age and specific usage was unavailable. The 3D laser scanning data and the DEM were used to determine tree heights in the model domains. The DEM was subtracted from the laser scanning data and buildings were clipped from the tree heights. A tree must be at least 3 m tall to be resolved by PALM. As PALM requires leaf area densities (LAD) for the plant canopy module, generic LAD profiles were applied to each tree depending on tree height and grid resolution. The applied LAD profiles are listed in S3 and S5 Tables for individual trees and S4 and S6 Tables for vegetation patches. The height and position of the trees are presented in S1 Fig. The trees have a conical shape. Soil type 3 (medium-fine porosity) was used in all domains. The input data for each domain was processed to the static driver netCDF file according to the PALM input data standard.

Evaluation

The model results from the microscale runs were compared to professional and crowdsourced air temperature data and evaluated. The 2 m potential air temperature was saved as a model output from PALM. 2 m air temperature was calculated from the 2 m potential air temperature. Areas containing buildings were clipped out of the results as the 2 m air temperature at building locations is the air temperature at 2 m above roof level. Then the time series of 2 m air temperature were extracted at every station’s location and at the surrounding nine grid cells for the parent domain and 24 grid cells for the child domain. All values surrounding a single station were averaged for every timestep. All data were written in a table with the timestep and station ID as identifiers. For the parent domain, all stations within 1 km of the domain boundaries were removed to exclude the influence of boundary effects on the results. The model results and the observational data were merged based on timestep and station ID. Missing observational values were filled with NAN values.

Several statistical methods are available to evaluate the model results with observational data. For this evaluation the following measures were chosen: arithmetic mean, standard deviation, Pearson correlation coefficient, coefficient of determination (R^2), root mean squared error (RMSE), mean squared error (MSE), index of agreement (IoA), and bias [55].

The statistical measures were calculated for the whole dataset and for four-hour time intervals. The graphical evaluation is based on boxplot time series and a direct comparison of each station's observations and the matching model results. The results can be used to evaluate overall model performance and differentiate model performance on a temporal and spatial basis.

Model results were prepared for evaluation using python version 3.8.10. Statistical evaluation was carried out with R version 4.1.2 [56] in RStudio [57] and maps were generated in QGIS 3.16 [58].

Results and Discussion

Model results

Fig 3 visualises the spatial and temporal development of the 2 m air temperature for four representative points in time. An animation of the air temperature with hourly timesteps for the whole simulation period is provided as S2 Fig. Early morning hours on the 8th of August show a stronger cooling of open and vegetated areas compared to built-up areas. After sunrise (05:00 UTC) air temperatures rise with a slight negative gradient from east to west. The morning hours are characterised by small air temperature differences, except for shaded areas and water surfaces which are cooler than surroundings. Air temperatures continue to rise until late afternoon (16:00 UTC). Air temperatures in built-up areas reach 34 to 36 °C. Simultaneously, air temperature differences between densely built-up and open areas increase with built-up areas showing higher air temperatures than open spaces. Air temperatures start to decline in the early evening (18:00 UTC) with a pronounced cooling in open and vegetated areas. After sunset (19:00 UTC) highest cooling rates are observed for open spaces while built-up areas cool down at a slower rate. Larger open and vegetated spaces show a stronger cooling than natural areas within built-up areas. The cooling process continues through the night. Air temperatures in built-up areas remain above 20 °C. The pattern of 2 m air temperature distribution reflects the surface properties such as the degree of imperviousness and presence of buildings.

Fig 3. Spatiotemporal pattern of the 2 m hourly averaged air temperature [°C] for the study area for the timesteps 08.08 05:00 h, 08.08 14:00 h, 08.08 20:00 h and 09.08 04:00 h.

Air temperature differences were calculated using the urban-rural air temperature difference. Rural areas were defined using the LCZ classification scheme by Stewart & Oke [59]. LCZ D (low plants) was defined as a rural area as standardised climate stations are placed on open fields. The required LCZ map was downloaded from the LCZ Generator [60]. The 2 m air temperature within LCZ D was averaged for every timestep and served as the rural reference air temperature. Air temperature differences for the domain and all timesteps were calculated. The resulting air temperature differences are visualised in Fig 4. An animation of the air temperature differences with hourly timesteps for the whole simulation period is provided as S3 Fig. Air temperature differences during the first modelled night clearly show the existence of an CLUHI. Air temperature differences decline in the first hours after sunrise starting at 05:00 UTC. Shaded areas are visible through their strongly negative temperature differences of up to -3 K or more. Exposed open areas in the southeast warm up quicker. Starting around 11:00 UTC built-up areas show higher temperatures than the rural reference. The built-up areas and exposed open spaces such as south-facing slopes show an increasing positive air temperature difference compared to the rural reference in the course of the midday and afternoon hours. North-facing slopes demonstrate negative air temperature differences in the same timeframe. The positive air temperature differences of built-up areas and sealed surfaces peak in the late afternoon and the first half of the second night. Open natural spaces cool down quicker resulting in a negative temperature difference. The model results show a strong CLUHI at night with built-up areas demonstrating air temperatures >4 K higher than the rural reference. Air temperature differences slightly decrease again in the second half of the night.

Fig 4. Spatiotemporal pattern of the hourly averaged urban-rural temperature differences [K] for the study area for the timesteps 08.08 05:00 h, 08.08 14:00 h, 08.08 20:00 h and 09.08 04:00 h.

Model evaluation

Evaluation with professional weather station data

2 m air temperature, relative humidity, and 10 m wind speed from PALM results were compared to measured values from the reference station for the child domain (Fig 5). Overall, modelled and observed air temperature, relative humidity and wind speed align well for the simulated period. Early morning air temperatures on the 8th of August are overestimated by around 3 to 5 K by PALM. Relative humidity is underestimated by the model. Measured warming after sunrise is stronger than modelled warming due to lower night-time and higher daytime air temperatures. Daytime modelled relative humidity is higher than observed relative humidity. After sunset, measured air temperatures show a stronger decrease than modelled air temperatures. Differences are highest at 22:00 UTC and decline from thereon. Towards the second half of the night modelled and measured air temperatures are well aligned. Differences in relative humidity correspond to the air temperature differences. Differences in wind speed are highest during morning hours on 8th August and in the afternoon. Differences between the model and the observation in the first hours could be caused by the model spinup. The model overestimates 10 m wind speed in the afternoon. This could be a reason for the underestimation of the 2 m air temperature as higher wind speeds induce better mixing and a reduction of air temperatures. Resler et al. [19] also observed a small overestimation of the wind speed with a generally good agreement. They attributed the overestimation to the limited spatial representativeness of point measurements. Nevertheless, the comparison shows an overall agreement between the model and the observation.

Fig 5. Comparison of the PALM 2 m air temperature [°C], relative humidity [%] and 10 m wind speed [m/s] to the observational data from the professional weather station LMSS for the timeframe 8th of August 02:00 h to 9th of August 05:00 h.

The modelled heat fluxes of the energy budget at the surface show a high latent heat flux and low ground and sensible heat fluxes (Fig 6). As the surface at the station is classified as tall grass in the model, the results are as expected. The high latent heat flux could explain the higher modelled relative humidity at midday. Two sources of uncertainties could cause the overestimated relative humidity. Soil moisture was supplied to the dynamic driver from the COSMO model. Due to the coarse resolution of the

COSMO model, small scale differences are neglected. A longer spinup period of more than 24 hours might reduce some of these uncertainties. The other uncertainty is the soil type provided to the model, as only one soil type was used in this setup. Soil moisture and heat transport within the soil and to the atmosphere depend on the soil type prescribed to the model [41]. While the model only has a low sensitivity to soil moisture in highly urbanised areas, the influence of soil moisture is significant in the vicinity of vegetation and natural surfaces [22]. Therefore, the difference between the designated soil type and the actual soil type at the measurement site can differ resulting in deviating energy fluxes a different relative humidity in the model.

Fig 6. Modelled energy fluxes separated into total energy flux (Q*), sensible heat flux (Q_H), latent heat flux (Q_E) and ground heat flux (Q_G) at the location of the LMSS station for the timeframe 8th of August 02:00 h to 9th of August 05:00 h.

Evaluation with crowdsourced air temperature data

The parent domain contains 59 Netatmo stations and the child domain nine Netatmo stations after the QC. Table 3 lists the values for all statistical parameters for the study area, divided by parent and child domain. The mean air temperature in the child domain is slightly higher in the modelled data (27.6 °C) than in the observed data (27.0 °C). In the parent domain mean air temperature of modelled and observed data is the same. Differences in standard deviation are small in both domains. The Pearson correlation coefficient, the R^2 and the IoA are close to their ideal values indicating a good agreement between modelled and observed data. These measures are slightly better for the parent domain. The bias for the parent domain is very small with 0.04. The negative bias for the child domain indicates a slight overestimation of the air temperature by the model. MSE and RMSE indicate disagreement between modelled and observed data. When reducing the stations used for evaluation of the parent domain to the stations within the child domain, the evaluation metrics for the parent domain are comparable to the child domain. The indicated better performance of the parent domain could be caused by the different sample sizes and the higher number of stations within the parent domain.

Table 3. Evaluation metrics for the study area, divided by parent and child domain for the air temperature [°C]

Child domain			**Parent domain**			**Parent domain, stations reduced to stations within child domain**		
	PALM	Netatmo		PALM	Netatmo		PALM	Netatmo
Mean [°C]	27.6	27.0	**Mean [°C]**	27.1	27.1	**Mean [°C]**	29.6	27.0
SD [°C]	5.0	4.8	**SD [°C]**	5.3	5.4	**SD [°C]**	5.3	4.8

Evaluation metrics					
Pearson r	0.93	**Pearson r**	0.93	**Pearson r**	0.93
R²	0.86	**R²**	0.88	**R²**	0.86
Slope	0.88	**Slope**	0.96	**Slope**	0.84
Intercept	2.71	**Intercept**	1.22	**Intercept**	4.3
RMSE	1.98	**RMSE**	1.89	**RMSE**	1.96
MSE	3.92	**MSE**	3.57	**MSE**	3.84
IoA	0.96	**IoA**	0.97	**IoA**	0.96
Bias	-0.53	**Bias**	0.04	**Bias**	0.1
n stations	9	**n stations**	59	**n stations**	9

A time series with boxplots visualises the temporal evolution of air temperature and the hourly variance for the study area (Fig 7). The temporal course of modelled and observed air temperature aligns well. During the first four hours modelled and observed data agree nicely. Air temperature increase in the morning is more pronounced in the modelled data than in the crowdsourced data though the alignment between model and observation improves at midday. While the timeseries reveals an underestimation of maximum daytime air temperatures in the parent domain, the maximum air temperature in the child domain is overestimated. This suggests a better representation of small-scale air temperature differences and extremes at a finer grid resolution. The small sample size in the child domain reduces the validity of the information. The late afternoon and early evening are characterised by an overestimation of air temperatures by the model, followed by a period of good agreement before the model underestimates night-time air temperatures. The boxplots indicate a higher variance in the observed air temperature data with a smaller variance for the modelled data. The child domain exhibits a higher variance of air temperature for the modelled data during midday. Both domains experience an underestimation of night-time air temperatures. This finding contrasts with the comparison of the model results to the data from the reference station indicating that one measurement location is not representative of the thermal conditions in urban areas. Comparable to the findings of Resler et al. [19], the diurnal cycle is well represented.

Fig 7. Boxplot time series of the PALM 2 m air temperature [°C] and Netatmo air temperature [°C] for the parent (left) and child (right) domain of the study area for the timeframe 8th of August 02:00 h to 9th of August 05:00 h.

The time series above show a temporal pattern of differences between the model and the observation. The data sets were split into four-hour time intervals to evaluate the temporal pattern of the air temperature differences. The resulting seven time intervals are: 08.08. 02:00 –05:00 (1), 08.08. 06:00 – 09:00 (2), 08.08. 10:00 – 13:00 (3), 08.08. 14:00 - 17:00 (4), 08.08. 18:00 – 21:00 (5), 08.08. 22:00 – 09.08. 01:00 (6), 09.08. 02:00 – 05:00 (7). The RMSE, IoA, bias, as well as mean air temperature and standard deviation, were calculated (Table 4). In both model domains, the model underestimates night-time air temperature in the second night as can be seen in the bias for time intervals six and seven. Air temperatures are overestimated by the model during the rest of the modelled period in the child domain while in the parent domain air temperatures are overestimated only during the morning and early evening. The measured air temperature range is higher than the modelled air temperature except for time interval six in both domains. Differences in standard deviation are highest at daytime (time intervals three and four) indicating higher spatial differences in air temperatures than calculated by the model. The IoA is highest for time intervals two, three and five showing a good representation of the warming process in the morning and the cooling process in the evening despite a high RMSE and differences in the absolute values.

Table 4. Evaluation metrics for the seven time intervals for the air temperature [°C], split by model domains.

Parent domain							
Timeslot	08.08 02:00 – 05:00	08.08 06:00 – 09:00	08.08 10:00 – 13:00	08.08 14:00 – 17:00	08.08 18:00 – 21:00	08.08 22:00 – 09.08 01:00	09.08 02:00 – 05:00
PALM mean	20.96	24.80	31.95	34.57	31.58	25.15	21.38
Netatmo mean	20.51	23.20	32.38	34.88	30.45	25.88	23.18
PALM SD	0.72	2.47	1.69	0.67	2.27	1.47	0.95
Netatmo SD	1.43	2.98	2.74	1.94	2.40	1.43	1.12
RMSE	1.40	2.36	2.14	1.89	1.73	1.42	2.13
IoA	0.56	0.82	0.74	0.41	0.86	0.75	0.47
Bias	-0.45	-1.60	0.43	0.31	-1.13	0.73	1.79
Child domain							

Timeslot	08.08 02:00 – 05:00	08.08 06:00 – 09:00	08.08 10:00 – 13:00	08.08 14:00 – 17:00	08.08 18:00 – 21:00	08.08 22:00 – 09.08 01:00	09.08 02:00 – 05:00
PALM mean	21.67	25.53	32.19	34.41	31.93	25.68	21.98
Netatmo mean	20.97	23.62	31.29	33.66	30.37	26.12	23.49
PALM SD	0.55	2.30	1.61	0.85	1.98	1.44	0.94
Netatmo SD	1.27	2.69	2.57	1.85	2.17	1.23	1.00
RMSE	1.41	2.25	2.45	2.38	2.05	1.25	1.77
IoA	0.51	0.82	0.60	0.13	0.78	0.76	0.51
Bias	-0.71	-1.91	-0.90	-0.75	-1.57	0.43	1.50

Some simplifications made in the preparation of the input data as well as the simple clear-sky radiation model could cause this temporal pattern of differences between the model and the observations.

A sensitivity analysis by Belda et al. [22] revealed high sensitivity of the air temperature to the presence or absence of trees. More trees reduce daytime air temperature while fewer trees reduce night-time air temperatures. Geletič et al. [18] showed air temperature reductions during the day in the vicinity of trees and at neighbourhood scale as an adaptation measure. The S1 Fig reveals that some Netatmo stations are in the vicinity of trees and could experience shading. The simplifications in the generation of LAD profiles made here could underestimate the shading caused by trees and therefore result in a higher daytime maximum air temperature as seen in the child domain and a lower night-time air temperature in both domains. An improved tree representation has the potential to reduce these differences. Tree representation could be improved by implementing a more sophisticated method to generate LAD profiles closer to reality following the method of Heldens et al. [61] or by exploring different remote sensing approaches described by Fassnacht et al [62].

The underestimation of night-time air temperatures in both domains could be attributed to the uncertainty of the thermal properties of buildings and pavements. Changing the building properties to model the effect of e.g. retrofitting results in significant changes of the ambient air temperature [23]. As shown by Belda et al. [22], the albedo, emissivity, thermal conductivity of walls and volumetric heat capacity have the highest sensitivity to changes. Sensitivity towards albedo is most important during the day due to its relation to the radiation balance while sensitivity towards emissivity and heat capacity is especially relevant at night for the energy balance. The current approach did not differentiate between commercial and residential buildings and building age. Furthermore, the used model version uses preliminary values for the thermal properties of the pavement types [41]. Improving information on the buildings could be achieved by relating the building position to the land use class as an approximation to the usage of the building and deriving the building age from the cadastral data of ALKIS for German cities as in Heldens et al. [61]. Material properties of the pavement types could be provided to the model via user-defined pavement types and albedo parameters in the static driver.

The clear-sky radiation model only considers radiation interactions at the surface [20]. Data on the cloud cover for the study period is provided by a professional weather station of the DWD in the neighbouring city of Essen [63]. Cloud cover is given in eighths (S4 Fig). On the 8th of August 2020, no cloud cover was observed until 22:00 UTC. A dense cloud cover developed until 01:00 UTC and solidified for the remainder of the night. The unresolved cloud cover in the model can be a reason for the underestimation of night-time air temperatures as the cloud cover increases longwave downward radiation and therefore reduces cooling. Furthermore, heating and cooling of the air caused by the divergence of radiative fluxes is missing in this approach [19]. An alternative to the clear-sky radiation model is the RRTMG model which is an external library to the PALM model. RRTMG provides information on the shortwave and longwave radiative heating rates for 1-D vertical columns [20]. This could improve the representation of radiative cooling in the night by the model [19]. Another alternative is including an external radiation scheme where downwelling shortwave and longwave radiation is provided to the model. Following this method, the effect of clouds can be considered in the simulations [19].

Comparing the modelled results with the observed data for every station individually in the parent domain (Fig 8) reveals potential sources of disagreement. The warming period in the morning has a lower density of observed data points. As the Netatmo sensors have a time lag for adjusting to rapidly changing temperatures, values from that period were likely filtered during the QC procedure due to the sensor lag. This is consistent with the study by Fenner et al. [29]. Air temperature at midday and afternoon is higher in the observed data of several stations. The form of the curve of some of these stations suggests that some radiation errors remain after the QC, e.g., stations 29023, 29261, 29270 and 160849. Stations with radiation errors either must be removed manually or stricter criteria can be set in QC level M2 and/or M5. Alternatively, the QC procedure must be developed further to improve the automated removal of radiation errors. Several stations without radiation error reveal an overestimation of air temperatures by the model at midday, such as stations 28994, 29031, 29440 and 154093. To the contrary, observed and modelled data align very well for other stations e.g., 29005, 29011, 29263, 29427 and 29586. Night-time air temperatures are underestimated at 39 of 59 stations in the parent domain. Reducing the number of stations to the child domain reveals a similar picture and is therefore not shown here. While for some stations the modelled and observed data align well, for other stations differences between the model and the observation are higher. Part of the disagreement could be attributed to missing data from the observations or radiation errors.

Fig 8. Timeseries of the PALM 2 m air temperature [°C] and Netatmo air temperature [°C] for each station individually for the parent domain for the timeframe 8th of August 02:00 h to 9th of August 05:00 h.

Independently of the QC procedure, the spatial representativeness of Netatmo data is relevant in the analysis. Netatmo stations are influenced by local- and micro-scale phenomena simultaneously. Their placement within urban areas results in the air temperature readings being influenced by the CLUHI effect [30]. In the present analysis, this is advantageous as the model is supposed to represent the CLUHI effect and the Netatmo data can reflect on the accuracy of the representation of the CLUHI in the model. As Netatmo stations are usually placed close to walls [31], their air temperature readings are influenced additionally by heat released from walls, resulting in higher air temperature measurements than a reference station at a further distance to buildings [29,31]. This could suggest an underestimation of the air temperature by the model, as in the present study at night-time, even though the deviation is possibly due to microscale effects on the individual Netatmo station. Therefore, one individual Netatmo station should not be used to evaluate the model results at a specific location. Simultaneously, studies using Netatmo data [28–31] have shown that spatial means and the sum of all stations give a reliable picture of the thermal environment. Therefore, several stations or all stations can be used for model evaluation. Due to their placement in urban areas, Netatmo stations usually do not cover natural areas like parks [29]. This is also the case in the present study where the analysis of the model performance is limited to built-up areas.

Further advantages are the usage of the same type of sensor for all stations [30] excluding differences based on sensor models and no observed sensor drift as shown by Meier et al. [30] and Fenner et al. [28].

The differences between the modelled and observed air temperature are mapped for representative points in time to evaluate the differences based on the stations' locations. Fig 9 shows the air temperature differences for the study area for four points in time. Throughout the day there is no clear pattern of under- or overestimation of a specific area. Air temperature differences between the model and the observation do not vary based on the density of the surrounding urban structure as stations in the city centre and in the suburbs both show higher and lower temperature readings than calculated by the model. In the second half of the second night, the model underestimates air temperatures over the whole domain. The differences between the model and the observation show a clearer pattern on the temporal scale while no pattern can be detected on a spatial scale.

Fig 9. Spatiotemporal pattern of the air temperature differences [K] between the PALM and Netatmo data for the study area for the timesteps 08.08 05:00 h, 08.08 14:00 h, 08.08 20:00 h and 09.08 04:00 h.

Aside from the above considerations on the model and the CWS, some general remarks on the computational costs and transferability of the method will be discussed. The mesoscale simulation used 126 CPU cores and the nested microscale simulations used 112 CPU cores. The runtimes were approx. 27 hours for the mesoscale simulation and 11 days and 4 hours for each microscale simulation. The mesoscale simulation could be run on a smaller machine with less CPU as the runtime in the present set-up is relatively short. Reducing the available CPU cores for the microscale simulation would result in an increased runtime. As an alternative, the simulation of the parent and child domains could be split where the results of the parent domain can be used as the dynamic input for the child domain as was done with the mesoscale simulation. Nevertheless, this would reduce the transferability of the results and it could add an adjustment zone for the turbulence development in the child domain. An additional limitation to the transferability is the use of the COSMO-D2 data as dynamic input for the mesoscale simulation. As the COSMO-D2 or the newer ICON-D2 archive data are not freely available, a different data source such as the WRF model could be used when no access to the COSMO data is available. Results of a different mesoscale model will differ from the COSMO results leading to a changed dynamic input and therefore different results than in this setup. The input data for the static driver is freely available, making the description of the model domains transferable. The Netatmo data used for evaluation is also freely available through the Netatmo APIs [30]. Processing of the model results, evaluation of the results with crowdsourced data and visualisation were carried out with open-source software and programming languages.

Conclusions

The model results represent the air temperature differences between built-up and natural areas. Air temperature differences are highest in the early evening and throughout the night and lowest in the hours after sunrise. Comparing the model results to measurement data from a professional weather station and crowdsourced air temperature reveals a good model performance. Evaluation metrics such as the Pearson correlation coefficient and the R^2 are close to their ideal values indicating a good agreement between model and observation. However, the MSE and RMSE give higher weight to outliers and show a certain disagreement. Differences in model accuracy on a spatial basis could not be detected. On a temporal basis, the evaluation metrics suggest a slightly worse performance for the second night.

The model results and the evaluation enable answering the research questions in the following.

In the present study, does the PALM model display intraurban air temperature differences according to well-known principles of the urban climate?

The PALM model displays intraurban air temperature variations in this case study as presented in the mapped results in Fig 3 and Fig 4. Built-up areas are characterised by higher air temperatures compared to open or natural spaces. The air temperature differences between the urban and natural areas are higher at night following the theory behind the CLUHI [2].

Based on the evaluation with CWS data, can a temporal and/or spatial pattern in model accuracy be detected?

Model accuracy varies throughout the day. Compared to the crowdsourced air temperature data, the modelled air temperature has a lower range at nearly all times. The warming period in the morning and the cooling period in the afternoon and evening are characterised by an overestimation by the model. The overestimation in the morning is likely due to a known sensor lag of the Netatmo stations [30]. The IoA for both warming and cooling periods is high indicating a good representation of the pattern of the cooling and warming process. The model underestimates night-time air temperatures in the second night. The cause of the underestimation could be caused by the clear sky radiation model where clouds are neglected. Data from a nearby climate station of the DWD revealed a dense cloud cover in the second half of the second night which was not resolved in the model. While a temporal pattern in model accuracy was detected, this study did not find a temporal pattern in model accuracy.

How suitable are citizen weather station data for model evaluation?

Quality controlled crowdsourced air temperature data showed significant potential for model evaluation. Crowdsourced air temperature data have a high spatial resolution and are therefore capable of representing the thermal conditions in different urban environments [29,30]. The crowdsourced data used is freely available and require no additional effort in terms of measurement campaigns. The QC procedure filters most of the errors inherent in crowdsourced data. Nevertheless, radiation errors remain which must be considered during model evaluation. The differentiation between micro- and local-scale influences on the air temperature readings is complicated. Therefore, one individual station is not sufficient for model evaluation, but the information derived from several stations and/or all stations is suitable for model evaluation.

The model evaluation and the answered research questions allow an outlook for future applications of the model and crowdsourced air temperature data for model evaluation. Model results could be improved by refining the input data in terms of tree representation, building information, surface materials and soil type. Instead of applying the clear sky radiation model, the RRTMG model can be used to achieve more realistic radiation budgets. Finally, on the modelling side, the mesoscale model WRF could be used as dynamic input for the mesoscale run. WRF is an open-source model, and the newest version can incorporate the LCZ scheme as the land cover scheme to include the effect of urban areas in mesoscale models [64,65]. On the measurement side, improved QC of the crowdsourced data further filtering the radiation errors can improve data quality. Higher data quality reduces uncertainties in model evaluation caused by the crowdsourced data. Adding CWS manually above natural surfaces would enable the evaluation of model performance between natural and paved surfaces. Using Netatmo CWS instead of professional measurement equipment reduces costs and ensures comparability of the measurements as the sensors remain the same.

Acknowledgements

We wish to thank Jessica Lehmkühler, Lohmeyer GmbH, for advice on the preparation of the input data. Moreover, we would like to thank Jonas Kittner, Institute of Geography at Ruhr-University Bochum, for providing the crowdsourced air temperature data from the database and Charlotte Hüser, Institute of Geography at Ruhr-University Bochum, for proof reading.

We acknowledge support by the DFG Open Access Publication Funds of the Ruhr-University Bochum.

References

1. United Nations, Department of Economic and Social Affairs, Population Division. World UrbanizationProspects: The 2018 Revision (ST/ESA/SER.A/420). New York; 2019. Available from: https://population.un.org/wup/Publications/.

2. Oke TR, Mills G, Christen A, Voogt JA. Urban Climates. Cambridge: Cambridge University Press; 2017.
3. Oswald SM, Hollosi B, Žuvela-Aloise M, See L, Guggenberger S, Hafner W, et al. Using urban climate modelling and improved land use classifications to support climate change adaptation in urban environments: A case study for the city of Klagenfurt, Austria. Urban Climate 2020;31:100582.
4. Ambrosini D, Galli G, Mancini B, Nardi I, Sfarra S. Evaluating Mitigation Effects of Urban Heat Islands in a Historical Small Center with the ENVI-Met® Climate Model. Sustainability 2014;6(10):7013–29.
5. RIZWAN AM, DENNIS LY, LIU C. A review on the generation, determination and mitigation of Urban Heat Island. Journal of Environmental Sciences 2008;20(1):120–8.
6. Geletič J, Lehnert M, Krč P, Resler J, Krayenhoff ES. High-Resolution Modelling of Thermal Exposure during a Hot Spell: A Case Study Using PALM-4U in Prague, Czech Republic. Atmosphere 2021;12(2):175.
7. Heaviside C, Macintyre H, Vardoulakis S. The Urban Heat Island: Implications for Health in a Changing Environment. Curr Environ Health Rep 2017;4(3):296–305. PubMed PMID: 28695487.
8. Nazarian N, Krayenhoff ES, Bechtel B, Hondula DM, Paolini R, Vanos J, et al. Integrated Assessment of Urban Overheating Impacts on Human Life. Earth's Future 2022;10(8).
9. Kovats RS, Hajat S. Heat stress and public health: a critical review. Annu Rev Public Health 2008;29:41–55. PubMed PMID: 18031221.
10. IPCC, editor. The Physical Science Basis. Contribution of Working Group I to the Sixth Assessment Report of the Intergovernmental Panel on Climate Change: Cambridge University Press; 2021.
11. Deutscher Wetterdienst. Klimastatusbericht Deutschland Jahr 2020. Offenbach; 2021.
12. Mishra V, Ganguly AR, Nijssen B, Lettenmaier DP. Changes in observed climate extremes in global urban areas. Environ. Res. Lett. 2015;10(2):24005.

13. Wouters H, De Ridder K, Poelmans L, Willems P, Brouwers J, Hosseinzadehtalaei P, et al. Heat stress increase under climate change twice as large in cities as in rural areas: A study for a densely populated midlatitude maritime region. Geophys. Res. Lett. 2017;44(17):8997–9007.
14. Toparlar Y, Blocken B, Vos P, van Heijst G, Janssen WD, van Hooff T, et al. CFD simulation and validation of urban microclimate: A case study for Bergpolder Zuid, Rotterdam. Building and Environment 2015;83:79–90.
15. Crank PJ, Sailor DJ, Ban-Weiss G, Taleghani M. Evaluating the ENVI-met microscale model for suitability in analysis of targeted urban heat mitigation strategies. Urban Climate 2018;26:188–97.
16. Salata F, Golasi I, Lieto Vollaro R de, Lieto Vollaro A de. Urban microclimate and outdoor thermal comfort. A proper procedure to fit ENVI-met simulation outputs to experimental data. Sustainable Cities and Society 2016;26:318–43.
17. van der Berg A. Climate Adaptation Planning for Resilient and Sustainable Cities: Perspectives from the City of Rotterdam (Netherlands) and the City of Antwerp (Belgium). Eur. j. risk regul. 2022:1–19.
18. Geletič J, Lehnert M, Resler J, Krč P, Middel A, Krayenhoff ES, et al. High-fidelity simulation of the effects of street trees, green roofs and green walls on the distribution of thermal exposure in Prague-Dejvice. Building and Environment 2022;223:109484.
19. Resler J, Eben K, Geletič J, Krč P, Rosecký M, Sühring M, et al. Validation of the PALM model system 6.0 in a real urban environment: a case study in Dejvice, Prague, the Czech Republic. Geosci. Model Dev. 2021;14(8):4797–842.
20. Maronga B, Banzhaf S, Burmeister C, Esch T, Forkel R, Fröhlich D, et al. Overview of the PALM model system 6.0. Geosci. Model Dev. 2020;13(3):1335–72.
21. Maronga B, Gross G, Raasch S, Banzhaf S, Forkel R, Heldens W, et al. Development of a new urban climate model based on the model PALM – Project overview, planned work, and first achievements. metz 2019;28(2):105–19.
22. Belda M, Resler J, Geletič J, Krč P, Maronga B, Sühring M, et al. Sensitivity analysis of the PALM model system 6.0 in the urban environment. Geosci. Model Dev. 2021;14(7):4443–64.

23. Maronga B, Winkler M, Li D. Can Areawide Building Retrofitting Affect the Urban Microclimate? An LES Study for Berlin, Germany. Journal of Applied Meteorology and Climatology 2022;61(7):800–17.
24. Fröhlich D, Matzarakis A. Calculating human thermal comfort and thermal stress in the PALM model system 6.0. Geosci. Model Dev. 2020;13(7):3055–65.
25. Harlan SL, Brazel AJ, Prashad L, Stefanov WL, Larsen L. Neighborhood microclimates and vulnerability to heat stress. Soc Sci Med 2006;63(11):2847–63. PubMed PMID: 16996668.
26. Muller CL, Chapman L, Johnston S, Kidd C, Illingworth S, Foody G, et al. Crowdsourcing for climate and atmospheric sciences: current status and future potential. Int. J. Climatol. 2015;35(11):3185–203.
27. Vulova S, Meier F, Fenner D, Nouri H, Kleinschmit B. Summer Nights in Berlin, Germany: Modeling Air Temperature Spatially With Remote Sensing, Crowdsourced Weather Data, and Machine Learning. IEEE J. Sel. Top. Appl. Earth Observations Remote Sensing 2020;13:5074–87.
28. Fenner D, Bechtel B, Demuzere M, Kittner J, Meier F. CrowdQC+—A Quality-Control for Crowdsourced Air-Temperature Observations Enabling World-Wide Urban Climate Applications. Front. Environ. Sci. 2021;9.
29. Fenner D, Meier F, Bechtel B, Otto M, Scherer D. Intra and inter 'local climate zone' variability of air temperature as observed by crowdsourced citizen weather stations in Berlin, Germany. metz 2017;26(5):525–47.
30. Meier F, Fenner D, Grassmann T, Otto M, Scherer D. Crowdsourcing air temperature from citizen weather stations for urban climate research. Urban Climate 2017;19:170–91.
31. Napoly A, Grassmann T, Meier F, Fenner D. Development and Application of a Statistically-Based Quality Control for Crowdsourced Air Temperature Data. Front. Earth Sci. 2018;6.
32. Venter ZS, Brousse O, Esau I, Meier F. Hyperlocal mapping of urban air temperature using remote sensing and crowdsourced weather data. Remote Sensing of Environment 2020;242:111791.

33. Regionalverband Ruhr (RVR). Metrople Ruhr - Die Stadt der Städte [Internet] [cited 2022 Mar 16]. Available from: https://metropole.ruhr/metropole.
34. Deutscher Wetterdienst (DWD). Großwetterlage August 2020 [Internet]. Offenbach: ; 2020. Available from: https://www.dwd.de/DE/leistungen/grosswetterlage/2020/grosswetterlage.html;jsessionid=9EDECA9C79507DAD5935E119A988C928.live21071?nn=16102.
35. Netatmo. Technische Details der Smarten Wetterstation [Internet] [cited 2021 Nov 1]. Available from: https://www.netatmo.com/de-de/weather/weatherstation/specifications.
36. Deardorff JW. Stratocumulus-capped mixed layers derived from a three-dimensional model. Boundary-Layer Meteorol 1980;18(4):495–527.
37. Moeng C-H, Wyngaard JC. Spectral Analysis of Large-Eddy Simulations of the Convective Boundary Layer. J. Atmos. Sci. 1988;45(23):3573–87.
38. Saiki EM, Moeng C-H, Sullivan PP. Large-Eddy Simulation Of The Stably Stratified Planetary Boundary Layer. Boundary-Layer Meteorology 2000;95(1):1–30.
39. Wicker LJ, Skamarock WC. Time-Splitting Methods for Elastic Models Using Forward Time Schemes. Mon. Wea. Rev. 2002;130(8):2088–97.
40. Maronga B, Gryschka M, Heinze R, Hoffmann F, Kanani-Sühring F, Keck M, et al. The Parallelized Large-Eddy Simulation Model (PALM) version 4.0 for atmospheric and oceanic flows: model formulation, recent developments, and future perspectives. Geosci. Model Dev. 2015;8(8):2515–51.
41. Gehrke KF, Sühring M, Maronga B. Modeling of land–surface interactions in the PALM model system 6.0: land surface model description, first evaluation, and sensitivity to model parameters. Geosci. Model Dev. 2021;14(8):5307–29.
42. Resler J, Krč P, Belda M, Juruš P, Benešová N, Lopata J, et al. PALM-USM v1.0: A new urban surface model integrated into the PALM large-eddy simulation model. Geosci. Model Dev. 2017;10(10):3635–59.

43. Salim MH, Schubert S, Resler J, Krč P, Maronga B, Kanani-Sühring F, et al. Importance of radiative transfer processes in urban climate models: a study based on the PALM 6.0 model system. Geosci. Model Dev. 2022;15(1):145–71.
44. Baldauf M, Gebhardt C, Theis S, Ritter B, Schraff C. Beschreibung des operationellen Kürzestfristvorhersagemodells COSMO-D2 und COSMO-D2-EPS und seiner Ausgabe in die Datenbanken des DWD. 1st ed.; 2018. Available from: https://www.dwd.de/SharedDocs/downloads/DE/modelldokumentationen/nwv/cosmo_d2/cosmo_d2_dbbeschr_version_1_0_201805.pdf?__blob=publicationFile&v=3.
45. Institut für Meteorologie und Klimatologie. INIFOR - Mesoscale Interface for Initializing and Forcing PALM [Internet]. Gottfried Wilhelm Leibniz Universität Hannover; 2020 [cited 2021 Nov 15]. Available from: https://palm.muk.uni-hannover.de/trac/wiki/doc/app/iofiles/inifor.
46. Xie Z-T, Castro IP. Efficient Generation of Inflow Conditions for Large Eddy Simulation of Street-Scale Flows. Flow Turbulence Combust 2008;81(3):449–70.
47. Kadasch E, Sühring M, Gronemeier T, Raasch S. Mesoscale nesting interface of the PALM model system 6.0. Geosci. Model Dev. 2021;14(9):5435–65.
48. Hellsten A, Ketelsen K, Sühring M, Auvinen M, Maronga B, Knigge C, et al. A nested multi-scale system implemented in the large-eddy simulation model PALM model system 6.0. Geosci. Model Dev. 2021;14(6):3185–214.
49. Digitales Geländemodell Gitterweite 200 m (DGM200); 2021. Available from: https://gdz.bkg.bund.de/index.php/default/digitale-geodaten/digitale-gelandemodelle/digitales-gelandemodell-gitterweite-200-m-dgm200.html.
50. Digitales Geländemodell - Gitterweite 1m (XYZ); 2021. Available from: https://www.bezreg-koeln.nrw.de/brk_internet/geobasis/hoehenmodelle/digitale_gelaendemodelle/index.html.
51. 3D-Messdaten Laserscanning (LAS); 2020. Available from: https://www.bezreg-koeln.nrw.de/brk_internet/geobasis/hoehenmodelle/3d-messdaten/index.html.
52. 3D-Gebäudemodell LoD1 (CityGML); 2021. Available from: https://www.bezreg-koeln.nrw.de/brk_internet/geobasis/3d_gebaeudemodelle/index.html.

53. Urban Atlas 2018; 2020. Available from: https://land.copernicus.eu/local/urban-atlas/urban-atlas-2018?tab=download.
54. CORINE land cover 2018; 2020. Available from: https://land.copernicus.eu/pan-european/corine-land-cover/clc2018?tab=download.
55. Bennett ND, Croke BF, Guariso G, Guillaume JH, Hamilton SH, Jakeman AJ, et al. Characterising performance of environmental models. Environmental Modelling & Software 2013;40:1–20.
56. R Core Team. R: A Language and Environment for Statistical Computing. Vienna, Austria; 2021.
57. RStudio Team. RStudio: Integrated Development Environment for R. Boston, MA; 2021.
58. QGIS Development Team. QGIS Geographic Information System; 2022.
59. Stewart ID, Oke TR. Local Climate Zones for Urban Temperature Studies. Bulletin of the American Meteorological Society 2012;93(12):1879–900.
60. Demuzere M, Kittner J, Bechtel B. LCZ Generator: A Web Application to Create Local Climate Zone Maps. Front. Environ. Sci. 2021;9.
61. Heldens W, Burmeister C, Kanani-Sühring F, Maronga B, Pavlik D, Sühring M, et al. Geospatial input data for the PALM model system 6.0: model requirements, data sources and processing. Geosci. Model Dev. 2020;13(11):5833–73.
62. Fassnacht FE, Latifi H, Stereńczak K, Modzelewska A, Lefsky M, Waser LT, et al. Review of studies on tree species classification from remotely sensed data. Remote Sensing of Environment 2016;186:64–87.
63. DWD Climate Data Center. Stündliche Stationsmessungen des Bedeckungsgrades in Achtel für Deutschland, Version v21.3; 2021 [cited 2021 Aug 4]. Available from: https://cdc.dwd.de/portal/.
64. Skamarock WC, Klemp JB, Dudhia J, Gill DO, Liu Z, Berner J, et al. A Description of the Advanced Research WRF Model Version 4; 2019.
65. Weather Research and Forecasting Model. GitHub - wrf-model/WRF: The official repository for the Weather Research and Forecasting (WRF) model [Internet]; 2021 [cited 2022 Mar 7]. Available from: https://github.com/wrf-model/WRF/releases/tag/v4.3.

Supporting information

S1 Fig. Tree height derived from the difference of the DEM and 3D laser scanning data as basis for the LAD profiles and the location of the Netatmo stations used for evaluation

S2 Fig. Animation of the PALM 2 m hourly averaged air temperature [°C] for the complete simulation period

S3 Fig. Animation of the PALM 2 m hourly averaged air temperature differences [K] for the complete simulation period

S4 Fig. Cloud cover in eighths as recorded by the professional weather station 'Essen-Bredeney' from the German Weather Service in the city of Essen, data extracted from DWD Climate Data Center [63]

S1 Table. Translation of Corine land cover classes to PALM vegetation, pavement and water types

S2 Table. Translation of Urban Atlas land use classes to PALM vegetation, pavement and water types

S3 Table. LAD profiles for single trees for the child domain with a resolution of 2.5 x 2.5 x 2.5 m

S4 Table. LAD profiles for vegetation patches (locations with vegetation type 7, deciduous broadleaf trees) for the child domain with a resolution of 2.5 x 2.5 x 2.5 m

S5 Table. LAD profiles for single trees for the parent domain with a resolution of 10 x 10 x 10 m

S6 Table. LAD profiles for vegetation patches (locations with vegetation type 7, deciduous broadleaf trees) for the parent domain with a resolution of 10 x 10 x 10 m

S7 Table. Server specifications

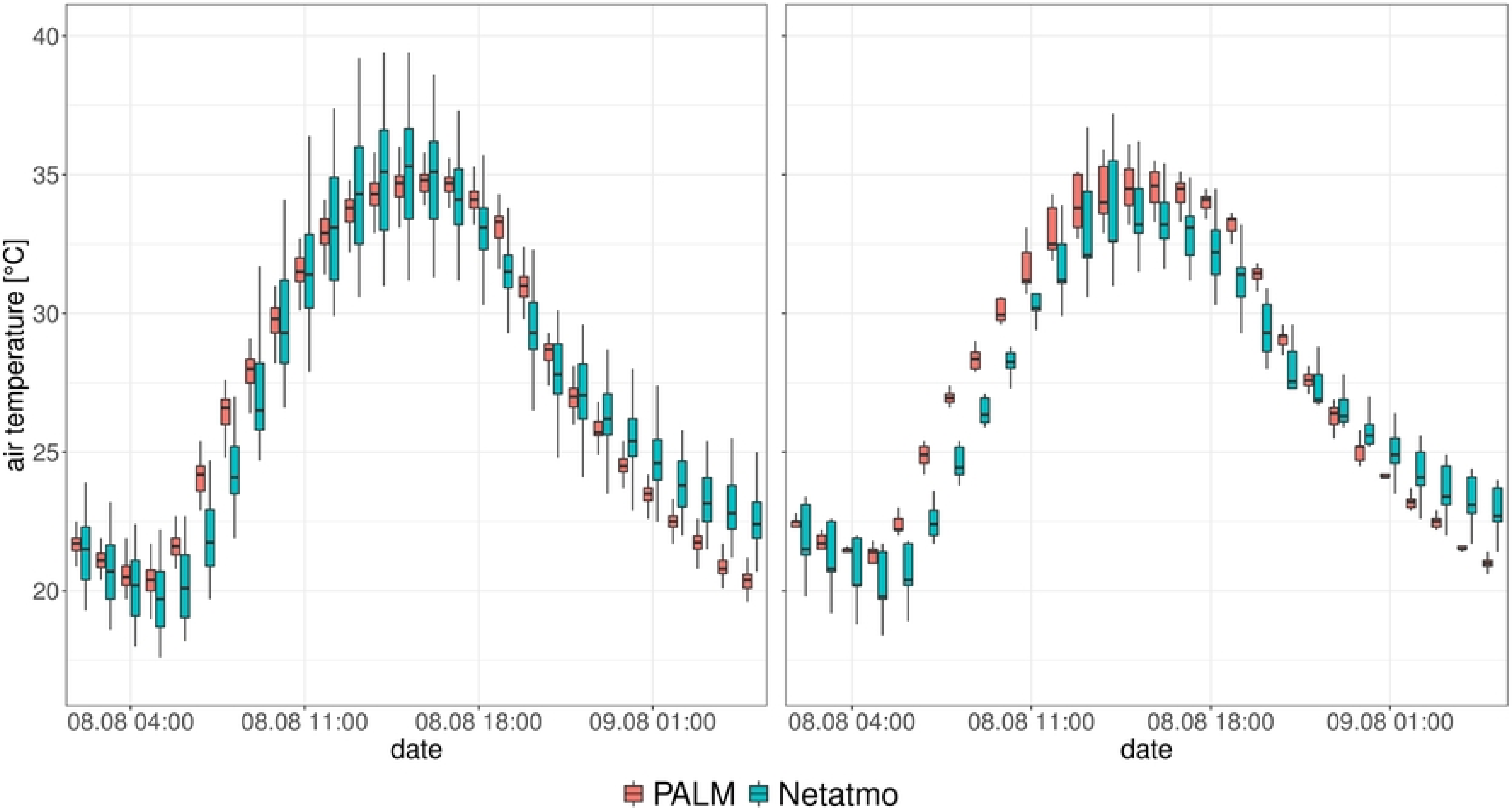
40
35
30
25
20
air temperature [°C]
08.08 04:00
08.08 11:00
08.08 18:00
09.08 01:00
date
PALM
Netatmo

Fig 7

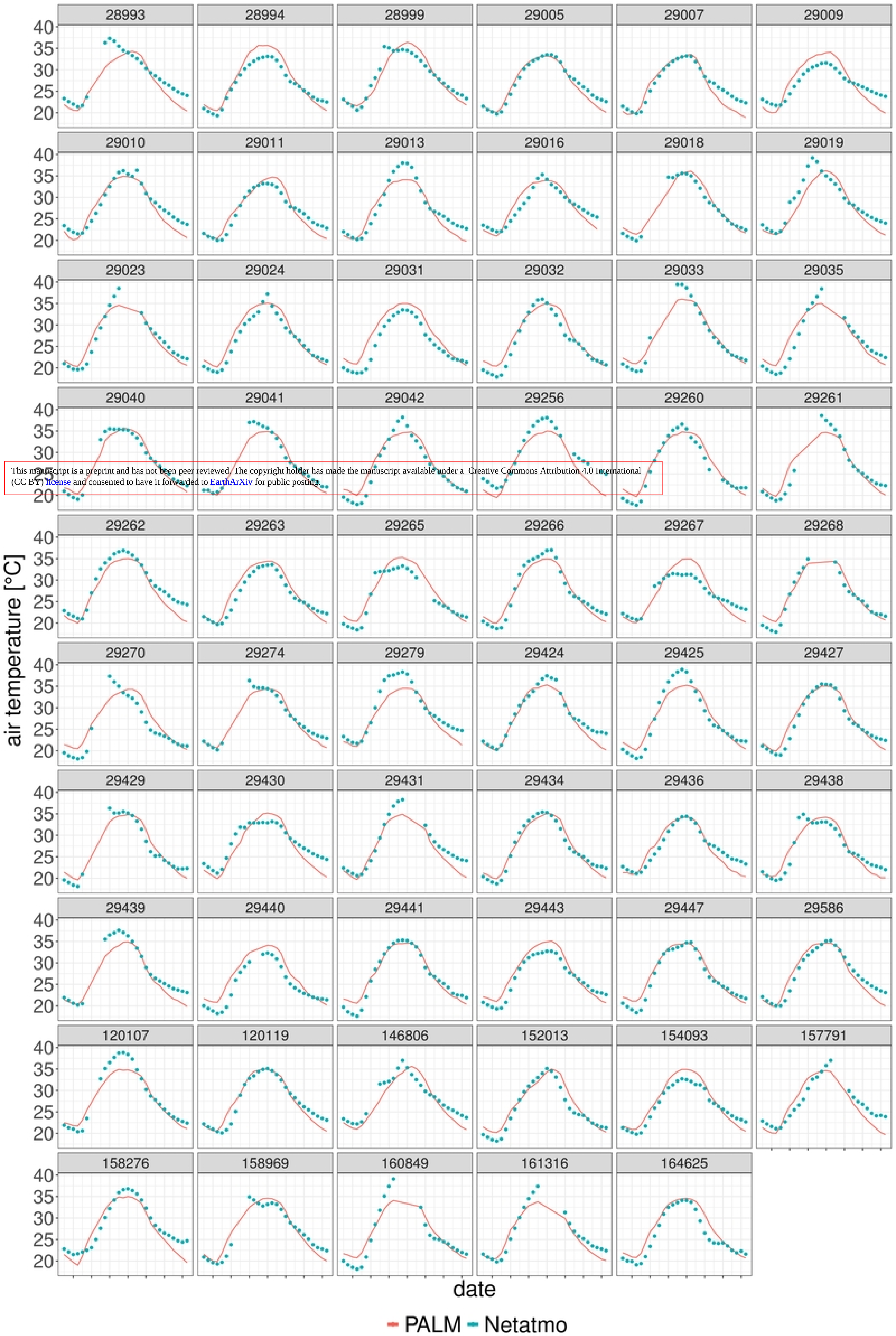

28993
28994
28999
29005
29007
29009
29010
29011
29013
29016
29018
29019
29023
29024
29031
29032
29033
29035
29040
29041
29042
29256
29260
29261
29262
29263
29265
29266
29267
29268
29270
29274
29279
29424
29425
29427
29429
29430
29431
29434
29436
29438
29439
29440
29441
29443
29447
29586
120107
120119
146806
152013
154093
157791
158276
158969
160849
161316
164625
40
35
30
25
20
air temperature [°C]
date
PALM
Netatmo

Fig 8

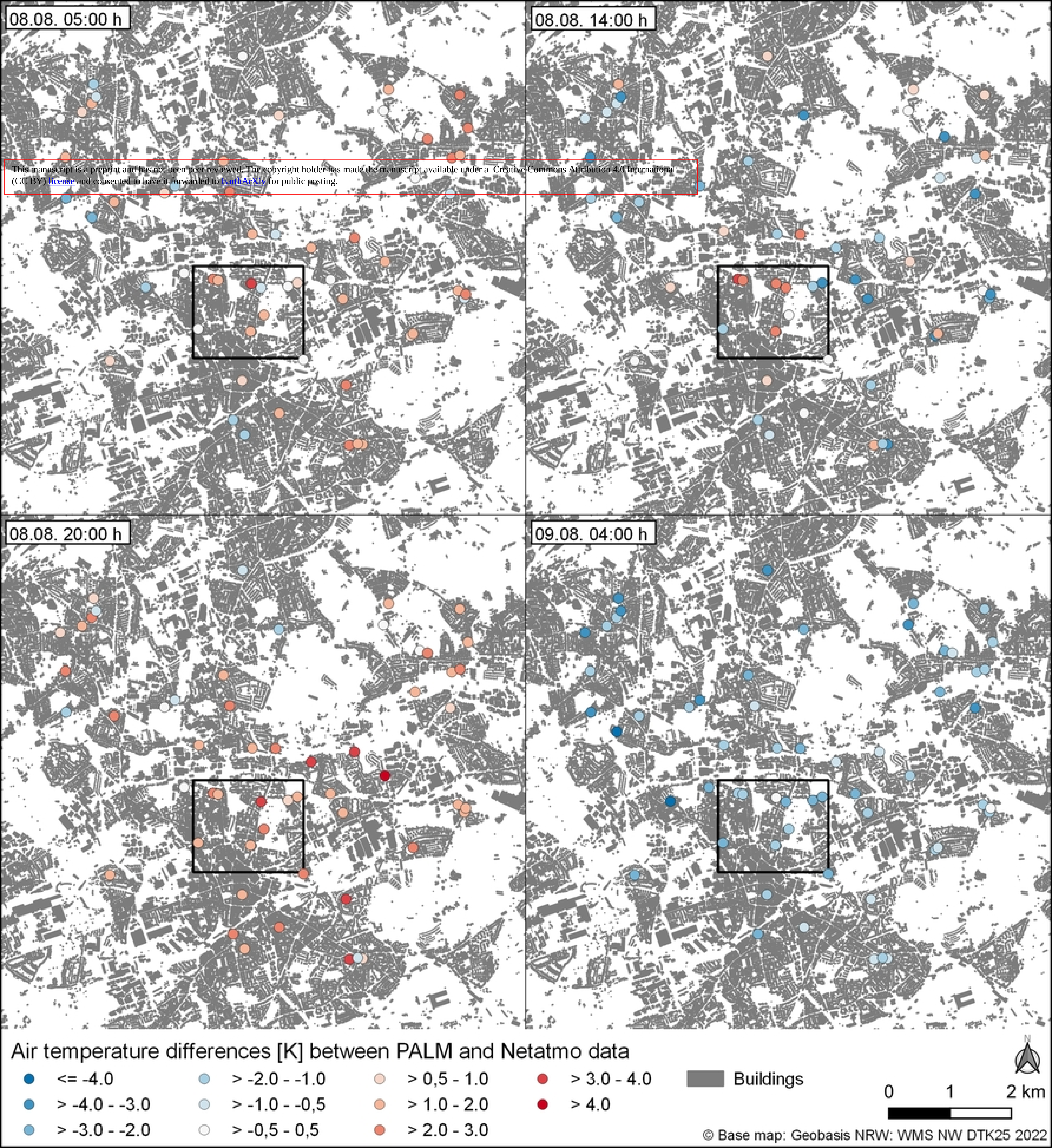
08.08. 05:00 h
08.08. 14:00 h
08.08. 20:00 h
09.08. 04:00 h
Air temperature differences [K] between PALM and Netatmo data
<= -4.0
> -4.0 - -3.0
> -3.0 - -2.0
> -2.0 - -1.0
> -1.0 - -0,5
> -0,5 - 0,5
> 0,5 - 1.0
> 1.0 - 2.0
> 2.0 - 3.0
> 3.0 - 4.0
> 4.0
Buildings
N
0
1
2 km
© Base map: Geobasis NRW: WMS NW DTK25 2022

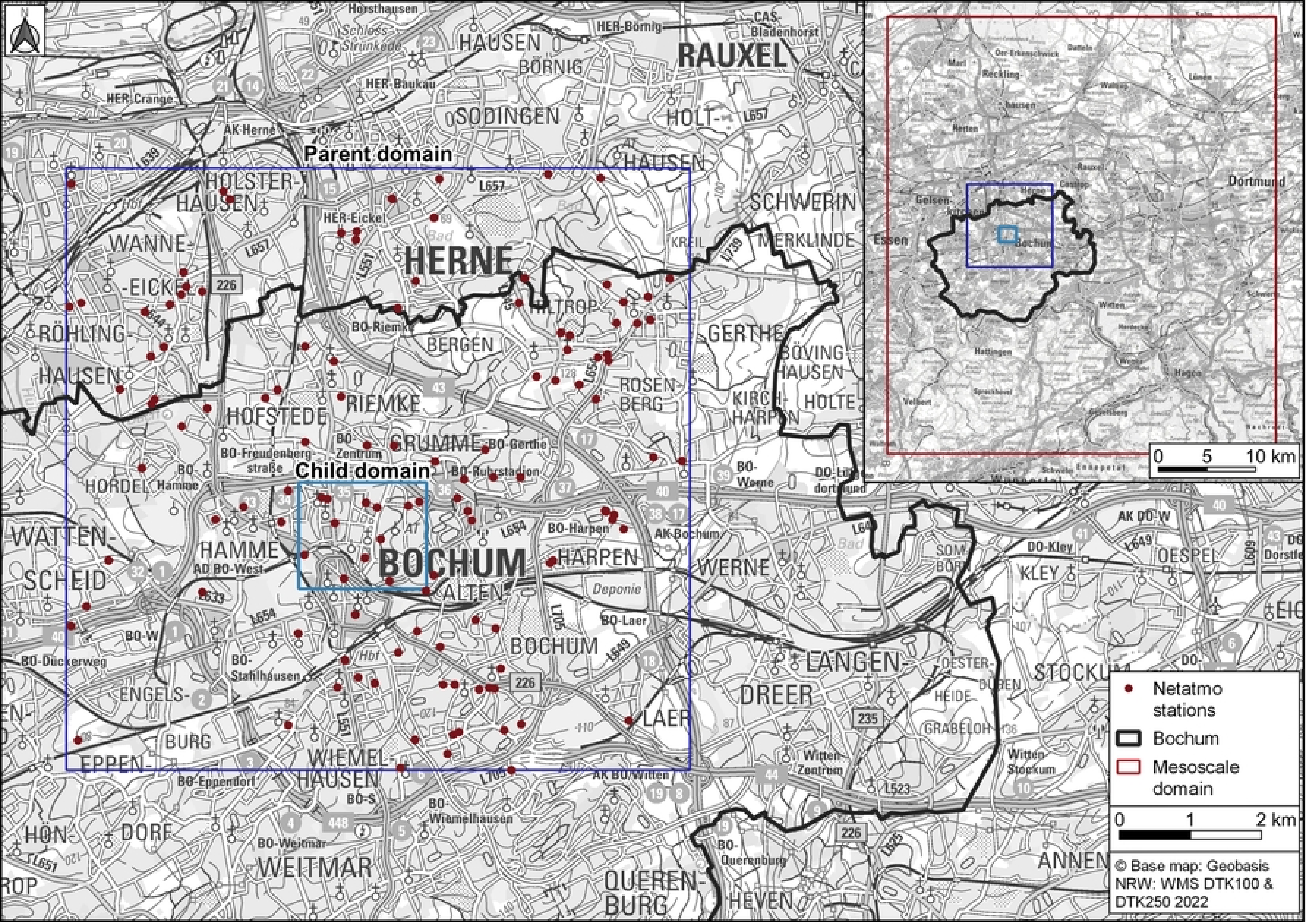
Parent domain
Child domain
Netatmo stations
Bochum
Mesoscale domain
0 1 2 km
0 5 10 km
© Base map: Geobasis NRW: WMS DTK100 & DTK250 2022
HERNE
BOCHUM
RAUXEL
HOLSTER-HAUSEN
WANNE-EICKEL
RÖHLING-HAUSEN
HOFSTEDE
RIEMKE
GRUMME
HAMME
HORDEL
WATTEN-SCHEID
HARPEN
ALTEN
WERNE
LANGEN-DREER
GERTHE
HILTROP
BERGEN
ROSEN-BERG
SODINGEN
BÖRNIG
HAUSEN
SCHWERIN
MERKLINDE
WIEMEL-HAUSEN
WEITMAR
LAER
STOCKUM
OESPEL
KLEY
EPPEN-
QUEREN-BURG
HEVEN
ENGELS-
BURG
Deponie
Essen
Dortmund

Fig 2

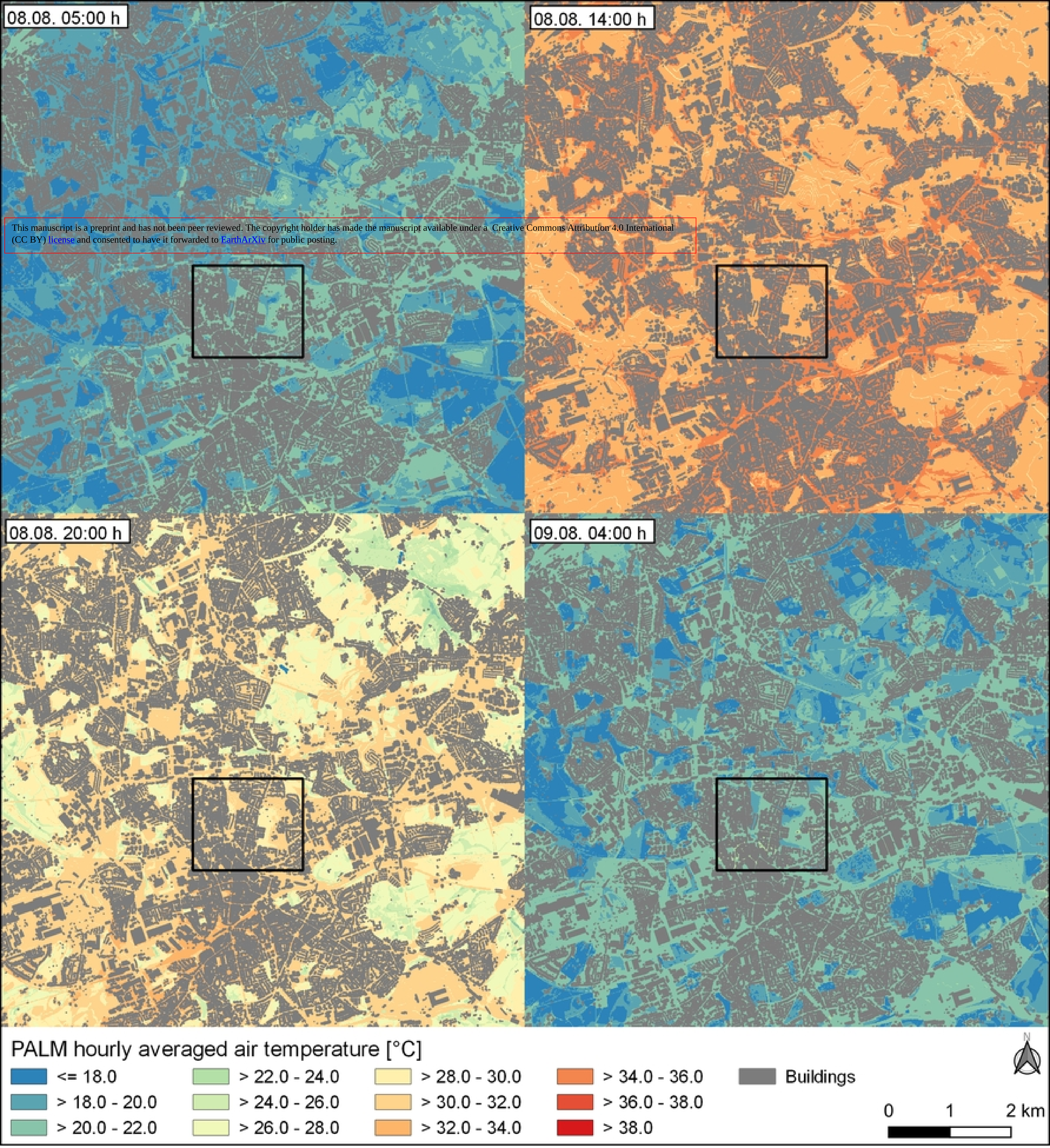
08.08. 05:00 h
08.08. 14:00 h
08.08. 20:00 h
09.08. 04:00 h
PALM hourly averaged air temperature [°C]
<= 18.0
> 18.0 - 20.0
> 20.0 - 22.0
> 22.0 - 24.0
> 24.0 - 26.0
> 26.0 - 28.0
> 28.0 - 30.0
> 30.0 - 32.0
> 32.0 - 34.0
> 34.0 - 36.0
> 36.0 - 38.0
> 38.0
Buildings
N
0
1
2 km

Fig 3

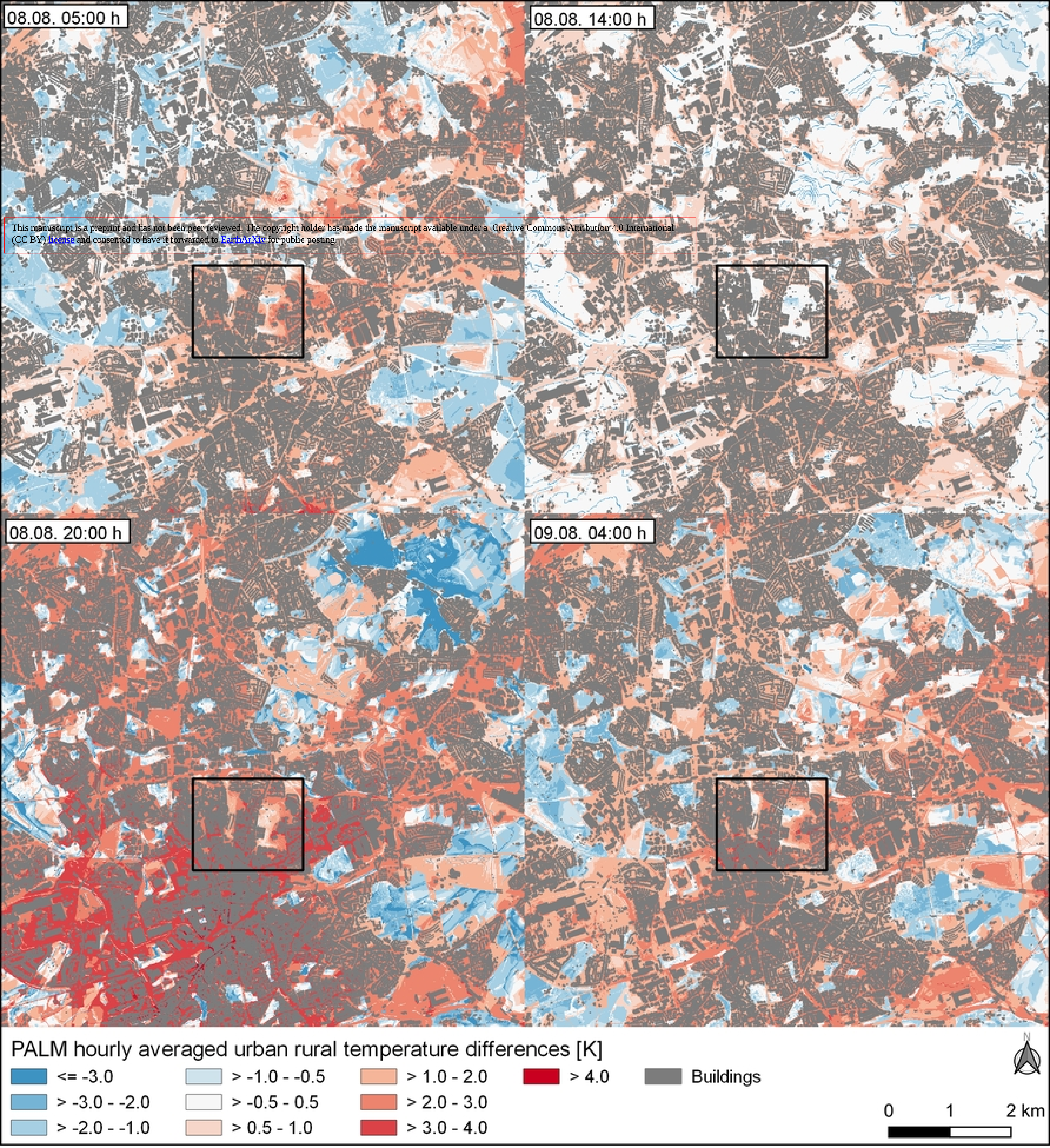
08.08. 05:00 h
08.08. 14:00 h
08.08. 20:00 h
09.08. 04:00 h
PALM hourly averaged urban rural temperature differences [K]
<= -3.0
> -3.0 - -2.0
> -2.0 - -1.0
> -1.0 - -0.5
> -0.5 - 0.5
> 0.5 - 1.0
> 1.0 - 2.0
> 2.0 - 3.0
> 3.0 - 4.0
> 4.0
Buildings
N
0
1
2 km

Fig 4

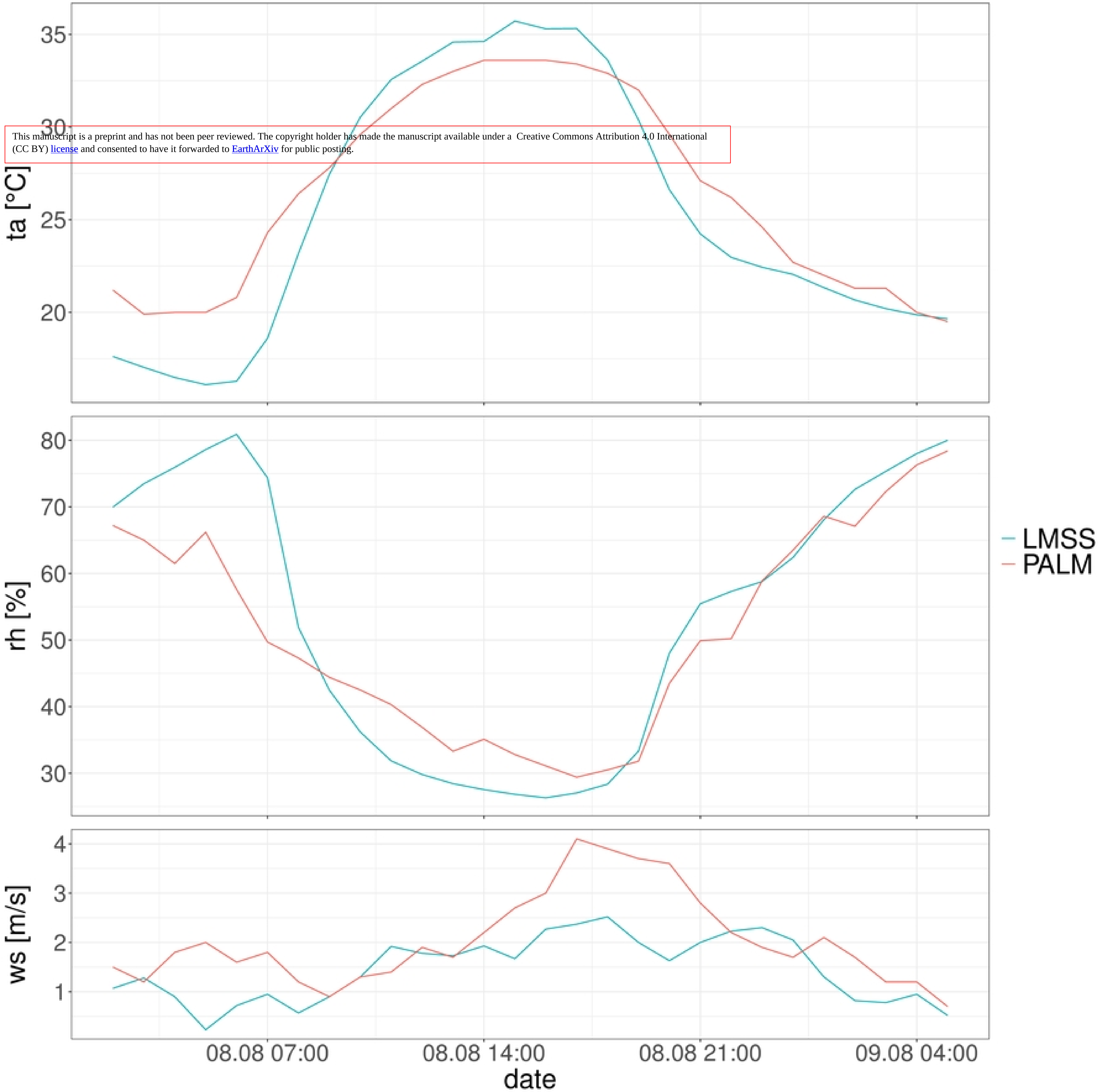

35
30
25
20
ta [°C]
80
70
60
50
40
30
rh [%]
4
3
2
1
ws [m/s]
08.08 07:00
08.08 14:00
08.08 21:00
09.08 04:00
date
LMSS
PALM

Fig 5

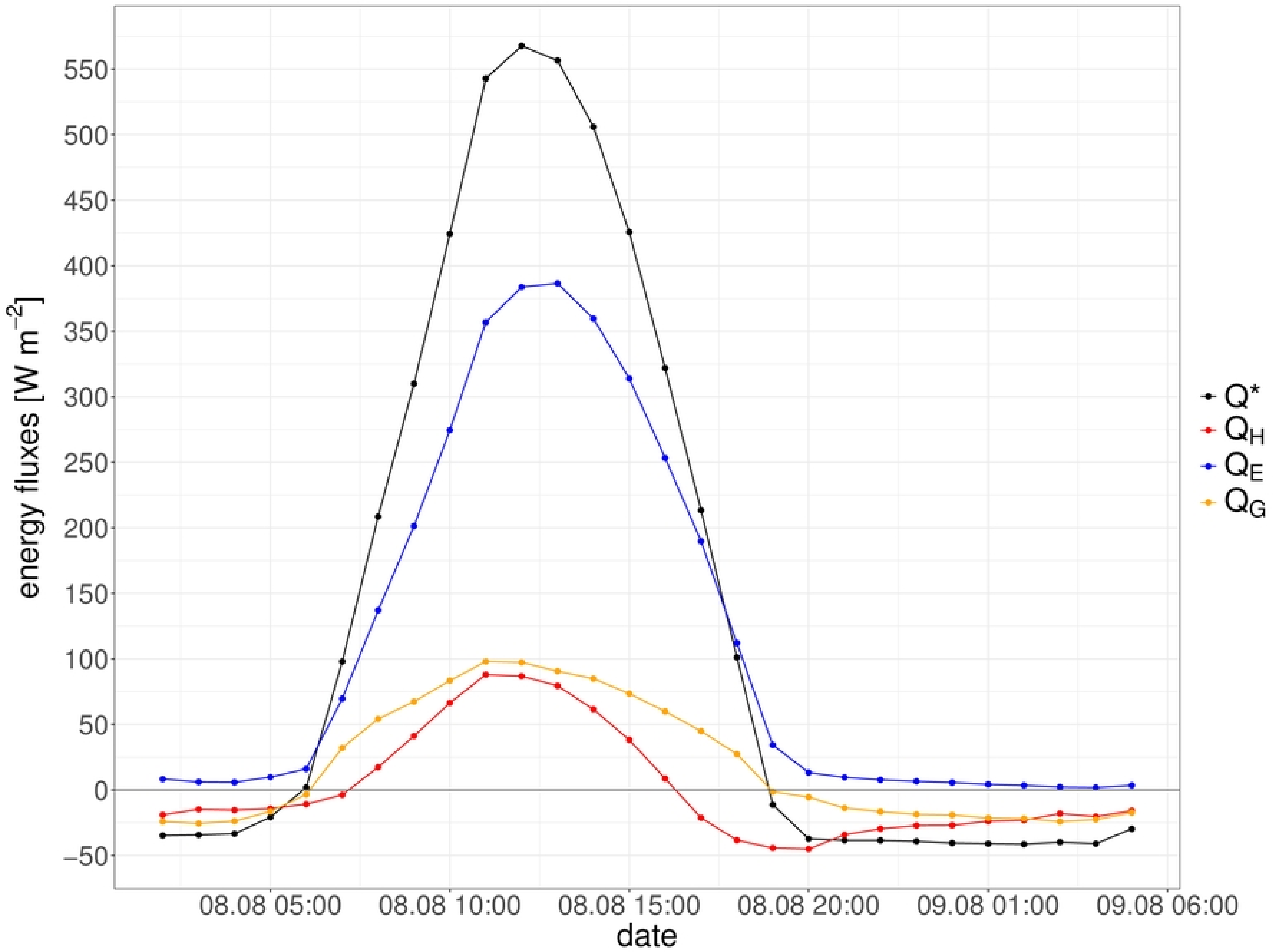

550
500
450
400
350
300
250
200
150
100
50
0
−50
energy fluxes [W m^{-2}]
08.08 05:00
08.08 10:00
08.08 15:00
08.08 20:00
09.08 01:00
09.08 06:00
date
Q*
Q_H
Q_E
Q_G

Fig 6

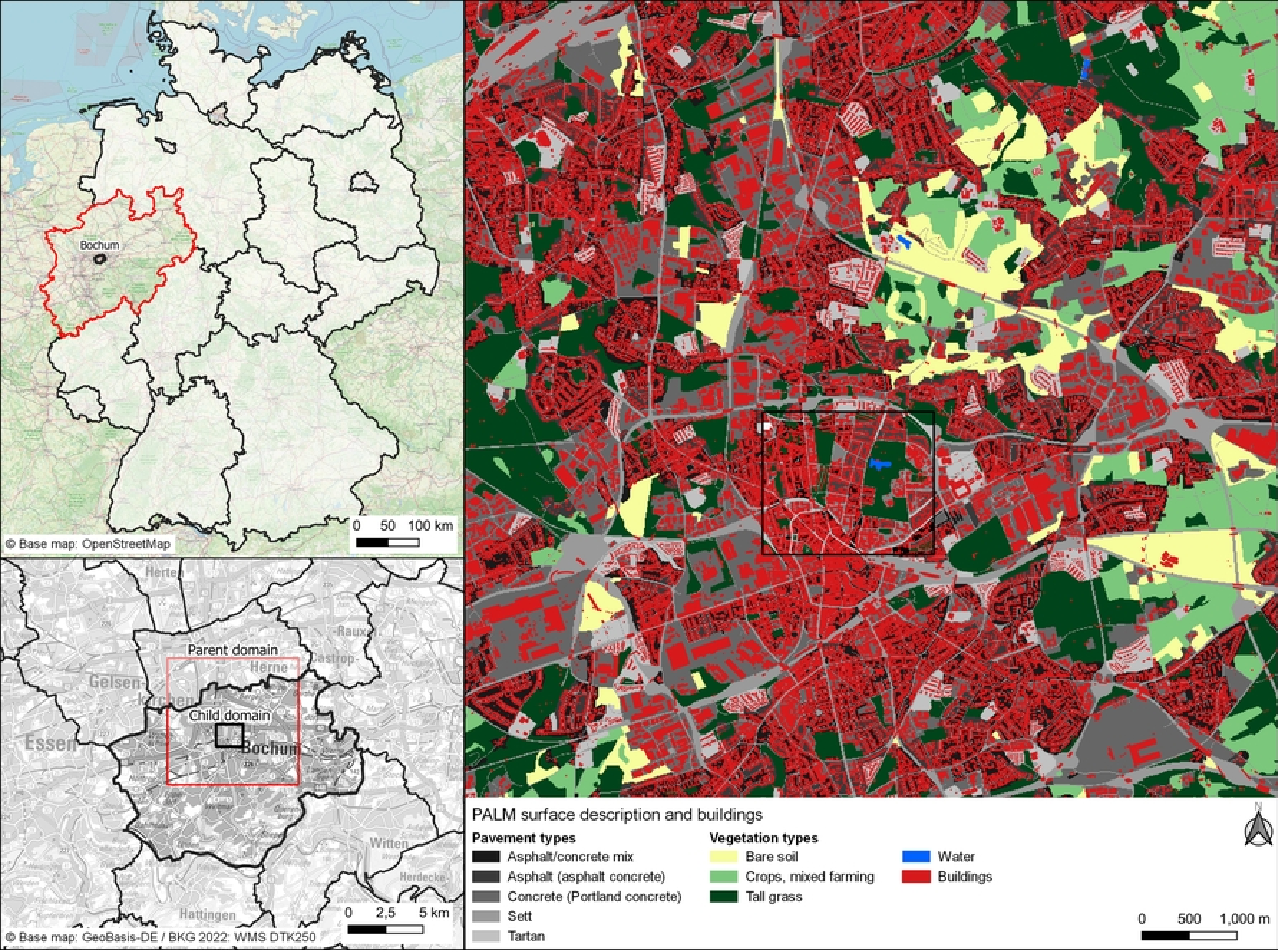
Bochum
0 50 100 km
© Base map: OpenStreetMap
Herten
Parent domain
Herne
Castrop-
Rauxel
Gelsen-
kirchen
Child domain
Essen
Bochum
Witten
Herdecke
Hattingen
0 2,5 5 km
© Base map: GeoBasis-DE / BKG 2022: WMS DTK250
PALM surface description and buildings
Pavement types
Asphalt/concrete mix
Asphalt (asphalt concrete)
Concrete (Portland concrete)
Sett
Tartan
Vegetation types
Bare soil
Crops, mixed farming
Tall grass
Water
Buildings
N
0 500 1,000 m

Fig 1